The Heat Transfer Coefficient associated with a Moving Packed Bed of Silica Particles Flowing through Parallel Plates.

Jeffrey Maskalunas, Gregory Nellis*, and Mark Anderson
Solar Energy Lab (SEL)
University of Wisconsin
1500 Engineering Drive
Madison, WI 53706

*corresponding author, gfnellis@engr.wisc.edu

Abstract

Concentrating Solar Power (CSP) with thermal energy storage has the potential to be a renewable energy technology with long duration, inexpensive energy storage. Higher temperature operation increases the conversion efficiency and reduces the cost of energy storage. Several emerging CSP designs utilize particles as the solar receiver due to their high temperature stability and low cost. In some designs, the particles are also used as the thermal energy storage (TES) media. In either configuration, an energy transfer is required between the hot particles and the working fluid in the power cycle in a Particle-to-Fluid Heat Exchanger (PtFHX). Understanding the heat transfer between a moving packed bed and a stationary surface is critical to the successful design of a PtFHX.

In this paper, a test facility is described in which a moving packed bed of silica sand with particle size 100 μm to 600 μm is introduced into the channel formed by two parallel plates, one of which is heated. The effective static thermal conductivity of the particles used for the test are separately measured over the entire range of test temperatures. The inlet and outlet bulk temperatures of the particle flow are measured as are the surface temperatures at several axial locations along the centerline of the plate. The result is the measurement of heat transfer coefficient as a function of temperature for several velocities. The uncertainty of the measurements is presented and the results are compared to model results found in the literature.

Keywords: concentrated solar power; thermal energy storage; particle; silica; heat transfer fluid; packed-bed flow

Research highlights of this article:

- The heat transfer coefficients associated with silica particles flowing in a rectangular channel are measured.
- The measurements are expressed in the form of a Nusselt number based on effective, static conductivity.
- The measurements are compared to theoretical predictions.

1. Introduction

Concentrating Solar Power (CSP) with thermal energy storage has the potential to be a renewable energy technology with long duration, inexpensive energy storage. Higher temperature operation increases the conversion efficiency and reduces the cost of energy storage. Several emerging CSP designs utilize particles as the solar receiver (Ho et al., 2018). The use of particles in this way is attractive due to their high temperature stability and low cost. In some designs, the particles are also used as the thermal energy storage (TES) media. In either of these configurations, an energy transfer is required between the hot particles and the working fluid in the power cycle. This energy transfer occurs in a Particle-to-Fluid Heat Exchanger (PtFHX). PtFHX designs fall broadly into two categories. Fluidized beds inject a flow of gas with the particles in order to "fluidize" the bed. Fluidization results in an improvement in the heat transfer coefficient on the particle-side (Gomez-Garcia et al., 2017), but has the disadvantages of requiring additional components and power consumption related to the fluidizing gas (compressors, recuperators, etc.) and can result in particle transport and carry over that can erode components. Moving packed beds utilize a gravity-driven flow of particles with no fluidizing gas at a high packing fraction. Moving packed bed PtFHX designs are a simple and cost-effective option for CSP applications (Ho et al., 2018).

In order to design and optimize PtFHX system it is necessary to understand the wall-to-moving bed heat transfer coefficient. There is less information regarding convection to a moving bed than convection to single phase fluid. Watkins, 2018 carried out a thorough study of heat transfer to dense granular flows, developing an apparatus in which a flow of sand was introduced into a long, straight tube. The wall-to-particle heat transfer was characterized in terms of typical convective flow quantities like Nusselt number and Graetz number that are themselves computed based on the static properties of the particle bed, the effective thermal conductivity and heat capacity. An experiment to measure the heat transfer coefficient in a moving packed bed flowing between parallel plates is also presented by Albrecht and Ho, 2018. There have been some PtFHX designs that are based on moving particle flow through parallel plate channels (Kirschmeier et al., 2020 and Albrecht and Ho, 2019). Based on the concept presented by Byman et al., 2014, the plates can be intermittently shifted or staggered so that the thermal boundary layer in the particles is disrupted. In this way, sequential banks of plates horizontally offset from one another can be used to reset the boundary layer and achieve a high heat transfer coefficient. Alaqel et al., 2020 present experimental results for a particle-to-air heat exchanger in which the particles fall over a staggered bank of tubes through which the fluid flows. Baumann and Zunft, 2015, present experimental results for a similar configuration.

The measurement of local heat transfer behavior in a particle flow is difficult because it requires that one set and precisely measure the heat flux at a surface and non-invasively and accurately measure both the local surface temperature and bulk temperature, all in a relatively harsh environment. As a result, there has been substantial effort related to simulating these flows. The discrete element method (DEM) (Cundal and Strack, 1979) has been used to simulate particle flow through various geometries that are relevant to heat exchangers and solar receivers. The DEM model is a complex Lagrangian approach in which the equations of motion and energy conservation are solved for every particle. It is computationally expensive and therefore of limited use for optimization and design studies. Continuum models treat the particle flow as a

continuum with a bulk velocity rather than tracking individual particles and therefore are much more computationally efficient. These models require some type of closure approach for the boundary conditions. These boundary effects are related to the increased thermal resistance associated with the layer of particles adjacent to the wall (Baskakov, 1964, Schlünder, 1984, and Tsotsas, 2010). The edge effects that are inherent to particle flow are concentrated in the wall-adjacent layer and are related to increased porosity near the wall and the relatively small number of wall-to-particle contacts that occur in a particle flow. The thermal conductance associated with the wall-adjacent layer depends strongly on the proximity of the particles with the wall. Morris et al., 2015, shows that this conductance is reduced by approximately 80% when the particle moves away from the wall by a distance that is 2% of the particle radius. In the same paper, a modification to the continuum models that accounts for wall-adjacent effects using a Nusselt number that represents the particle-to-wall thermal resistance in terms of the solid concentration is presented. This approach is shown to agree with the more complex DEM simulation results in Morris et al., 2016. Watkins, 2018 uses a similar approach in which the continuum is broken into two layers (the Two Layer Model): the bulk - where the effective conductivity is the bulk or static value and a wall adjacent layer that accounts for the lower solid concentration and lower effective conductivity near the wall. The details of the wall-adjacent layer depend on particle diameter, geometry, and flow rates and can be obtained using DEM simulations. Albrecht and Ho, 2017 present a model of a moving packed bed using this idea; the wall-adjacent layer is accounted for using a contact resistance calculated based on the particle diameter and the near-wall void fraction for a static particle bed.

This paper presents an experimental facility capable of measuring the heat transfer coefficient associated with a moving packed bed of silica particles flowing through a parallel plate channel with one heated wall. The effective conductivity and effective volume specific heat capacity of the silica particles under static conditions has been measured separately over the range of temperatures associated with the experiments in order to quantify any uncertainty relative to these parameters (Maskalunas, 2020 and Maskalunas et al.. 2020). The measurements include the rate of heating provided to the heated wall and the inlet and outlet bulk particle temperatures as well as the surface temperatures on both the heated and unheated walls at various locations. These measurements provide the heat transfer coefficient between the moving packed bed and the heated wall (based on the surface to bulk temperature difference). The uncertainty in the measured heat transfer coefficient and Nusselt number is presented. This work provides careful measurements of the behavior of well-characterized particles flowing through a simple flow channel that has not previously been presented. As a result, it is possible to estimate the impact of the wall-adjacent layer and compare with the modeling approach presented in the literature, specifically the model suggested by Albrecht and Ho, 2017. The particular configuration that was selected (i.e., parallel plates with one plate heated) simulates half a flow channel in proposed moving packed bed heat exchanger designs.

2. Experimental Testing

Test Facility

The test facility is shown in Figure 1. The facility is located in a 50 foot tall 20 foot diameter silo facility serviced by a crane for moving the sand. The sand hopper is positioned above the

second floor of the silo structure and filled with the particles to be tested. The test section is positioned below the hopper and empties into the basin which is placed on a scale. The particles are heated as they flow through the test section and therefore at the completion of a test the basin can be lifted and the hot particles transferred to the hopper for a subsequent run. Repeating this several times allows for testing at higher than ambient temperatures.

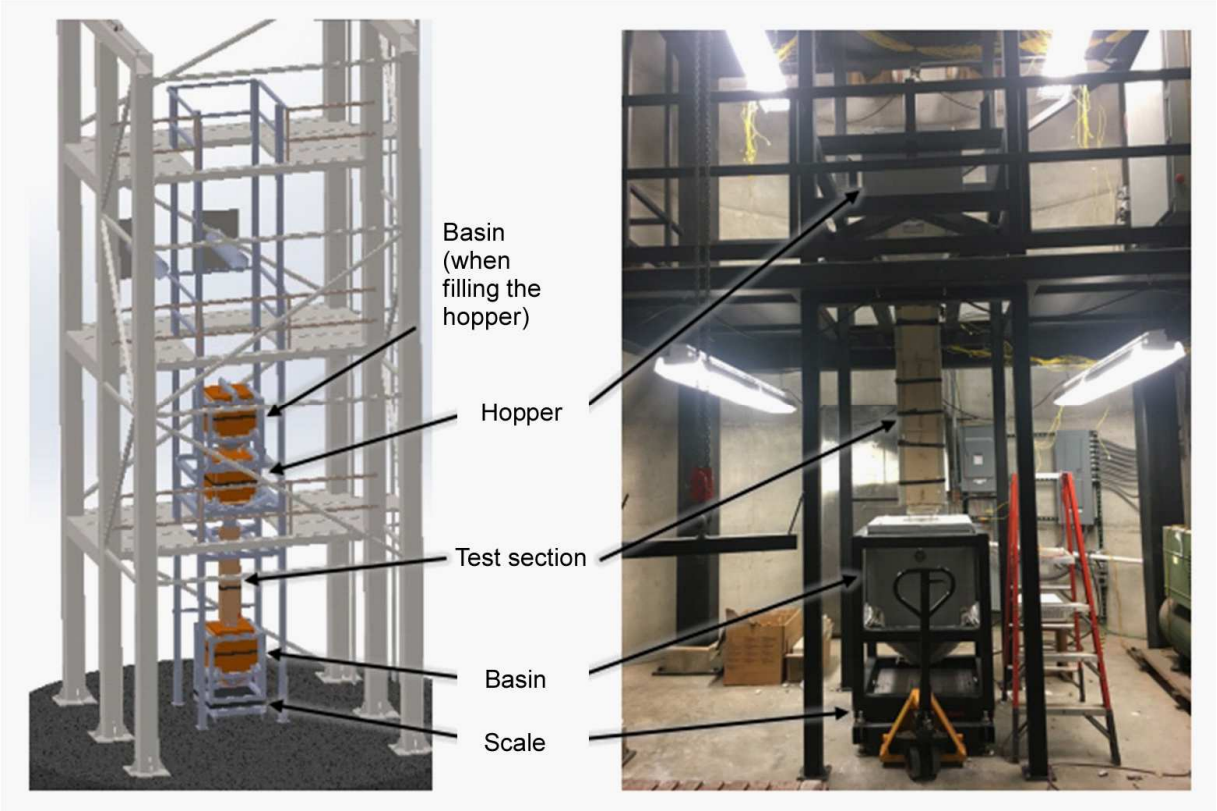

Figure 1: (Left) Rendering and (right) photograph of test facility. Test facility consists of a hopper filled with test particles above the test section emptying into the basin which is set on a scale.

The flow rate through the test facility is controlled by adjusting a flow control valve installed between the bottom of the test section and the basin. The valve consists of two plates, each with a series of 5.1 mm holes. Moving the valve to its fully open position aligns these holes while moving the valve to its fully closed position misaligns them. The flow rate is measured using the scale installed under the basin. The flow rate could be reliably controlled between a lower limit of approximately 18 g/s (or 18 mm/s) and 81 g/s (or 82 mm/s). The size of the hopper allows approximately 2 hours of continuous testing under most conditions.

The test section consists of two plates. Each plate is made of 316 stainless steel and is 1500 mm in the flow direction by 230 mm perpendicular to the flow direction. Mica spacers are installed in order to achieve a controlled 3 mm gap between the plates, as shown in Figure 2 (top). The dimension of the channel that is formed is 203 mm x 3 mm. One of the plates is heated by a serpentine heater located on its back-side capable of providing up to 3.2 kW of heating.

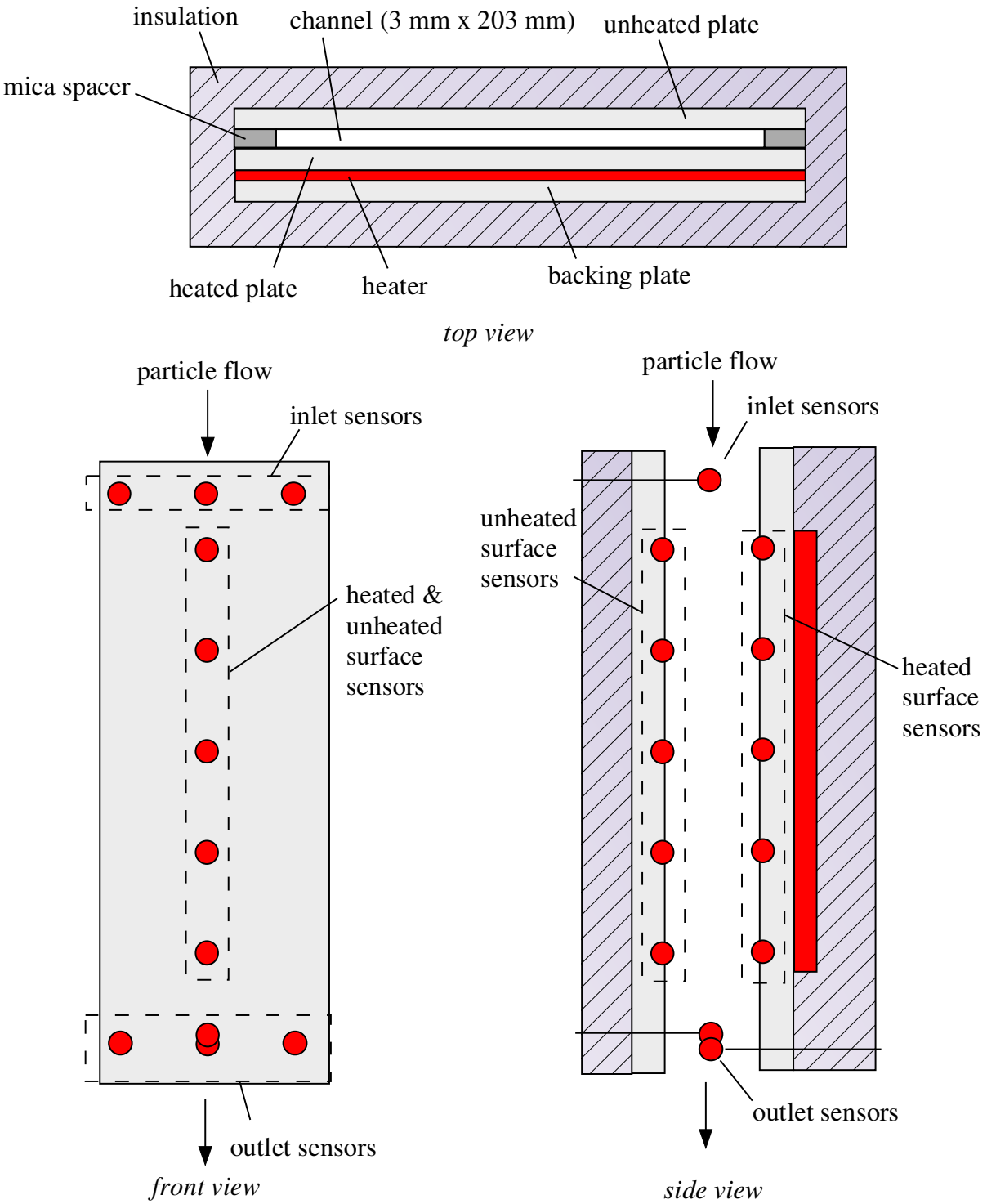

Figure 2: (top) Top view showing a cross-sectional view of the channel formed between the test section plates and (bottom) schematic showing the front and side views with the locations of the inlet, outlet, and surface temperature sensors indicated.

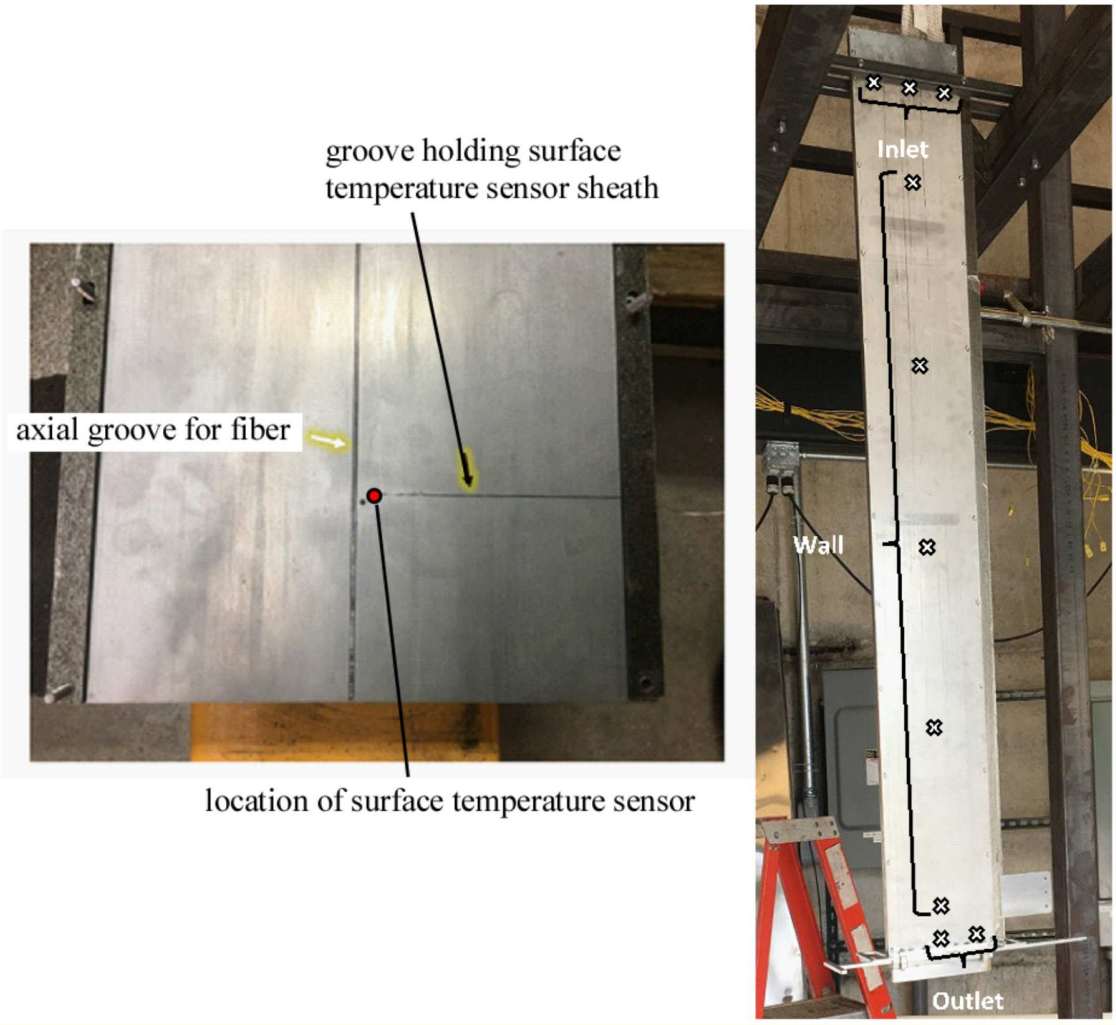

Figure 3: (Left) Photograph showing the groove in which the surface temperature sensor is press fit (note that the axial groove was not used but was installed in order to allow fiber-based temperature measurements) and (right) photograph of the unheated plate of the test section showing the location of the temperature sensors.

The surface temperature of each plate is measured along the center line of the channel, see Figure 2 (bottom) at five axial locations relative to the inlet of the heated section (x = 19 cm, 51 cm, 83 cm, 114 cm, and 146 cm); the heated surface temperature sensor closest to the inlet (at x = 19.1 cm) failed during testing and are therefore not reported. The surface thermocouples are installed by press-fitting the sheath into grooves that are milled into the plates on the sides exposed to the sand, as shown in Figure 3 (left). The inlet bulk temperature is measured using three thermocouples that are inserted into the sand flow just after the hopper. The outlet bulk temperature is measured using four thermocouples inserted in the sand; two of these enter through the heated plate (one at the center and one nearer the edge) and the remaining two enter through the unheated plate (also at the center and nearer the edge). The entire test section is insulated with 5 cm of Microtherm® insulation board in addition to Pyrogel and Kaowool in those locations where the Microtherm® could not be installed.

The characteristics and capabilities of the test facility are summarized in Table 1.

Table 1: Characteristics of Test Section

Characteristic	Symbol	Value	Uncertainty in value
Length in flow direction	L	152.4 cm	0.1 cm
Width perpendicular to flow direction	W	20.3 cm	0.1 cm
Gap height	g	3.0 mm	0.1 mm
Mass flow rate	$\dot{m}$	18 – 81 g/s	See Table 2
Heater power	$\dot{q}_e$	0 – 3.2 kW	See Table 2
Inlet temperature	T_{in}	0 - 170ºC	See Table 2

Measurement Uncertainty

The fundamental measurements made during testing together with the associated instrumentation and estimated uncertainty are summarized in Table 2. Additional details regarding the instrumentation can be found in Maskalunas, 2020.

Table 2: Measurements with instrumentation uncertainties.

Measurement	Symbol	Device	Instrumentation Uncertainty	Additional Experimental Uncertainty
Mass flow rate	$\dot{m}$	Rice Lake RoughDeck HP floor scale with Weigh-Tronix ZM303 indicator	0.3 g/s	1.0 g/s
Surface temperatures	T_s	Type K thermocouple	0.2 K[1]	0.5 K
Inlet bulk temperatures	T_{in}	Type K thermocouple	0.2 K[1]	5 K (preheated runs), 0.5 K (non-preheated runs)
Outlet bulk temperatures	T_{out}	Type K thermocouple	0.2 K[1]	5 K (all runs)
Electric power to heater	$\dot{q}_e$	Multimeter for voltage and power supply current measurement	10 W	-
Axial location of temperature sensors	x	Installed location of grooves	2 mm	-

1. Thermocouples were calibrated in a water bath after purchase.

The uncertainties provided in the fourth column of Table 2 are the instrumentation uncertainties. There are additional uncertainties inherent to the operation of the test facility. For example, the mass flow rate during a run would vary slightly as the valve plate occasionally became slightly blocked and then the blockage cleared. The measurement of the outlet bulk temperature tended to be sensitive to the location of the thermocouples within the channel due to temperature gradients in the particles; this led to an additional experimental uncertainty associated with this measurement. For runs in which the particles had been preheated by previous runs there tended to be temperature gradients associated with the sand in the hopper and therefore the inlet temperature would also vary throughout the run. There is an additional uncertainty in the surface

temperature related to the method used to mount them on the surface. The additional experimental uncertainty of each quantity is estimated and reported in the last column of Table 2.

Particles

The particles used for the testing are Wedron Silica #410, a high purity round grain silica sand available from Fairmount Minerals (accessed 2021). Silica 410 is more than 99.6% SiO_2 and consists of silica sand particles in the size range from 75 µm to 425 µm. The Sauter mean diameter of the sand is approximately 260 µm and the median particle size is approximately 240 µm. The bulk density of the sand was measured to be 1625 kg/m^3 by weighing a precise volume of the sand; this corresponds to a void fraction of approximately 38%. The effective thermal conductivity and heat capacity of the sand was measured using the static test facility discussed in Maskalunas, 2020. The measurements were made over the entire temperature range of interest and are shown in Figure 4. The uncertainty in the effective conductivity has been estimated to be 5% and the uncertainty in the specific heat capacity has been estimated to be 5% over the temperature range used in testing.

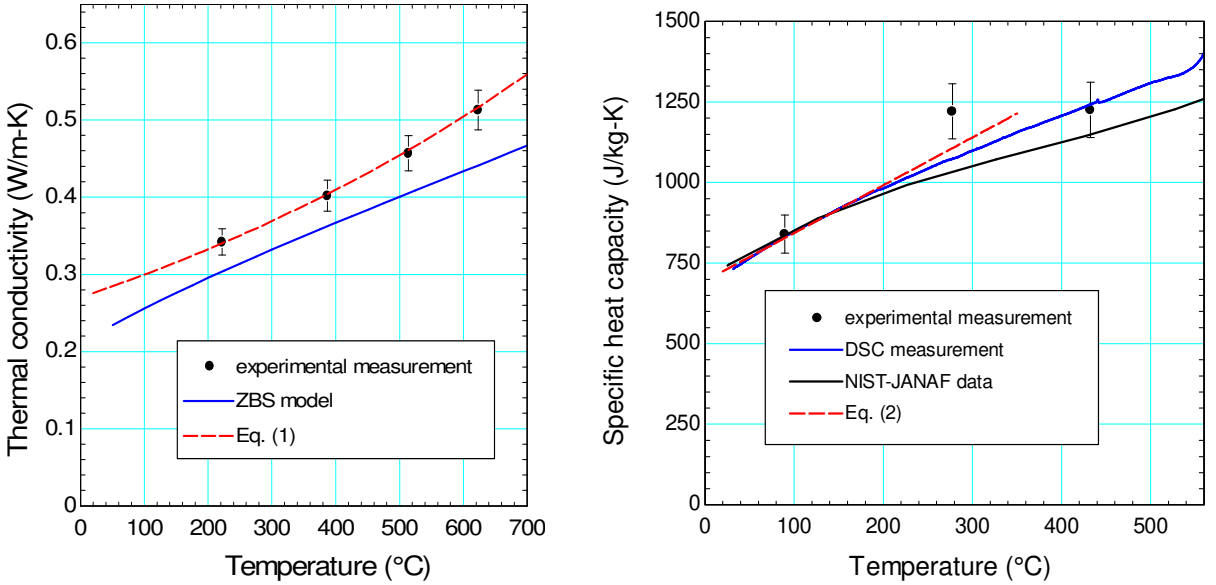

Figure 4: (Left) Effective static thermal conductivity of the Silica 410 sand measured in Maskalunas, 2020. Also shown is the thermal conductivity calculated using the Zehner, Bauer, and Schlűnder model (ZBS) model (van Antwerpen et al., 2010) assuming a emissivity of 0.8. (Right) Effective specific heat capacity of the Silica 410 sand measured in Maskalunas, 2020. Also shown is the results of measurements obtained from a sample using a differential scanning calorimeter and the data from NIST-JANAF for Quartz-Silica (NIST, 2020). Equations (1) and (2) are also shown.

The equations used to represent these measurements during data reduction are given below.

$$k = 0.270 \exp\left(0.00104T\right) \tag{1}$$

$$c = 694.8 + 1.484T \tag{2}$$

where k is conductivity in W/m-K, c is specific heat capacity in J/kg-K, and T is temperature in °C. The thermal conductivity curve was fit to the experimental measurements made using the static test rig while the specific heat capacity curve was fit to the DSC measurements below 200°C, the temperature range corresponding to the dynamic tests.

Tests

The experimental tests that were run are summarized in Table 3. The independent variables that could be controlled during testing were the flow rate (based on the position of the flow control valve), inlet temperature (based on whether the sand had been preheated), and heater power. Runs were taken sequentially throughout the testing (i.e., Run 1 was first and Run 36 last) while the data sets are groups of runs that were taken together (typically during a single day).

Table 3: Summary of tests.

Data Set/ Runs	Mass Flow Rate	Inlet Temperature	Heater Power	Notes
A/ 1-6,8	61-81 g/s	2-148°C	2.54–2.77 kW	Nominally constant flow rate and heat flux w/increasing inlet temp.
B/ 9-12	18–75 g/s	11-12°C	2.60-2.72 kW	Nominally constant inlet temp. and heat flux w/increasing flow rate
C/ 14-18	54-73 g/s	6.9-60°C	1.65-2.7 kW	Nominally constant flow rate w/varying inlet temp. and heat flux
D/ 21-23	27-64 g/s	19-20°C	2.65-2.71 kW	Nominally constant inlet temp. and heat flux w/increasing flow rate (approximately replicates Data Set B)
E/ 24-27	26-58 g/s	29-34°C	2.63-2.68 kW	Nominally constant inlet temp. and heat flux w/increasing flow rate (approximately replicates Data Set B)
F/ 28-31	30-33 g/s	5.4-5.8°C	0.2-2.7 kW	Nominally constant flow rate and inlet temp. w/increasing heat flux
G/ 32-36	27-64 g/s	9.9-167°C	2.5-2.7 kW	Nominally constant heat flux w/varying flow rate and increasing inlet temp.

Data were taken for each test run after the facility had reached a steady state, which typically occurred approximately 40 minutes after the initiation of flow.

3. Results

Data Reduction

Figure 5 illustrates the temperature measurements taken during Run 22 which was in Data Set D. The inlet and exit temperatures are shown (the measurements at the center of the channel are shown, with error bars to indicate their spread) as well as the temperatures on the heated and unheated surfaces.

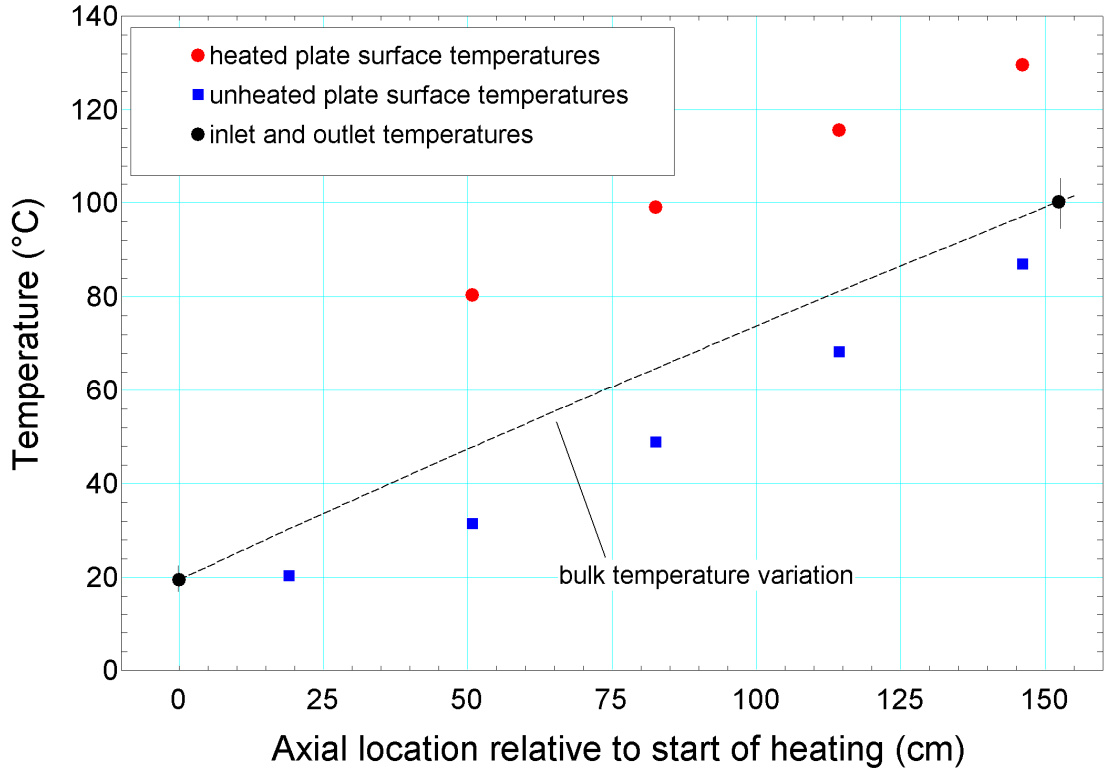

Figure 5: Temperature measurements taken during Run 22 in Data Set D (T_{in} = 19.5ºC, u = 43.3 mm/s, $\dot{m}$= 42.9 g/s, $\dot{q}''$ = 8.76 kW//m^2). Also shown is the bulk temperature variation estimated assuming constant heat flux with the specific heat capacity variation given in Eq. (2).

The local heat transfer coefficient is calculated based on the difference between the local heated surface to bulk temperature difference:

$$h = \frac{\dot{q}''}{\left(T_{s,H} - T_b\right)} \tag{3}$$

where $T_{s,H}$ is the heated surface temperature, T_b is the bulk temperature, and $\dot{q}''$ is the heat flux. The local Nusselt number is defined according to:

(4)

where g is the channel height and k is the effective conductivity of the sand. Notice in Figure 5 that towards the inlet of the test section the unheated surface temperature tends to match the inlet temperature. Once the flow becomes fully developed, the unheated surface temperature tends to increase linearly as it follows the bulk temperature. The heated surface temperature also tends to increase linearly due to the relatively constant heat transfer coefficient in the fully developed

region. The distance required for the flow to become fully developed can be estimated approximately according to:

$$x_{fd,t} \approx \frac{g^2 \rho c u}{4k} \tag{5}$$

where u is the bulk velocity and ρ and c are the bulk density and effective specific heat capacity of the sand. For the conditions associated with the highest velocity flows the thermal entry length is approximately 70 cm and therefore the final three surface temperature measurements are consistently in the fully developed region.

In order to calculate the local heat transfer coefficient, the bulk temperature was estimated based on the specific enthalpy. The specific enthalpy (i) assumed to vary linearly from inlet to outlet, which is consistent with a constant heat flux applied by the electrical heater. The specific enthalpy as a function of temperature is obtained by integrating Eq. (2) assuming a reference temperature of 0ºC.

$$i = \int_0^T c(T)\,dT = 694.8T + 1.484\frac{T^2}{2} \tag{6}$$

Using Eq. (6), the inlet and outlet specific enthalpy (i_{in} and i_{out}) are calculated using the inlet and outlet temperatures, respectively; note that the temperatures located at the center of the test section are used for this. The specific enthalpy is computed at any axial location according to:

$$i(x) = i_{in} + (i_{out} - i_{in})\frac{x}{L} \tag{7}$$

The specific enthalpy at each temperature sensor location can then be used to estimate the bulk temperature at that location using Eq. (6). The dashed line in Figure 5 is the estimated bulk temperature variation for Run 22; note that because the specific heat capacity is relatively constant over the temperature range, the bulk temperature variation is close to linear. The rate of heating provided to the particles is estimated using an energy balance on the test section:

$$\dot{q} = \dot{m}(i_{out} - i_{in}) \tag{8}$$

The bulk temperature measured at the outlet is sensitive to the location of the temperature sensor within the channel because a temperature gradient persists at this location. The outlet temperature sensors were positioned in the center of the channel at the midpoint between the heated and unheated surfaces; one entered from the heated side and the other from the unheated side. The bulk outlet temperature is the average of these two measurements. The result using this technique was double checked in two ways. First, the rate of heating computed using Eq. (8) is within 10% of the electrical power provided by the heater. Second, the rate of heating matches the temperature gradient that was measured using the surface temperatures mounted on the heated and unheated walls in the fully developed region to within 10%. The heat flux used to

calculate the heat transfer coefficient is the ratio of the heat transfer to the particles computed using an energy balance and the heated area of the passage:

$$\dot{q}'' = \frac{\dot{m}\left(i_{out} - i_{in}\right)}{W\,L} \tag{9}$$

The conductivity used to compute the Nusselt number at each location is computed using the bulk temperature at that location in Eq. (1). The measurements associated with the last three surface temperature sensors are averaged together to provide the single measurement of the fully developed heat transfer coefficient and Nusselt number associated with each run. The uncertainty values provided in Table 2 are propagated through the calculations to provide the uncertainty in these quantities.

Heat Transfer Coefficient and Nusselt Number Measurements

Data sets B, D, and E each carry out testing with a constant inlet temperature and constant heat flux but varying flow rates. These tests were meant to evaluate reproducibility as they are separated by several months. Figure 6 (left) illustrates the heat transfer coefficient as a function of the bulk velocity for each of these tests. The bulk velocity is computed according to:

$$u = \frac{\dot{m}}{W\,g\,\rho} \tag{10}$$

There is a gradual reduction in the heat transfer coefficient with velocity. This can be explained in part by the fact that the higher velocity tests occurred at a lower temperature (on average) due to the constant heat flux applied over the tests. Therefore, the sand had lower conductivity, as shown in Figure 4 (left). When presented in terms of Nusselt number in Figure 4 (right) the velocity dependence is reduced but is still present.

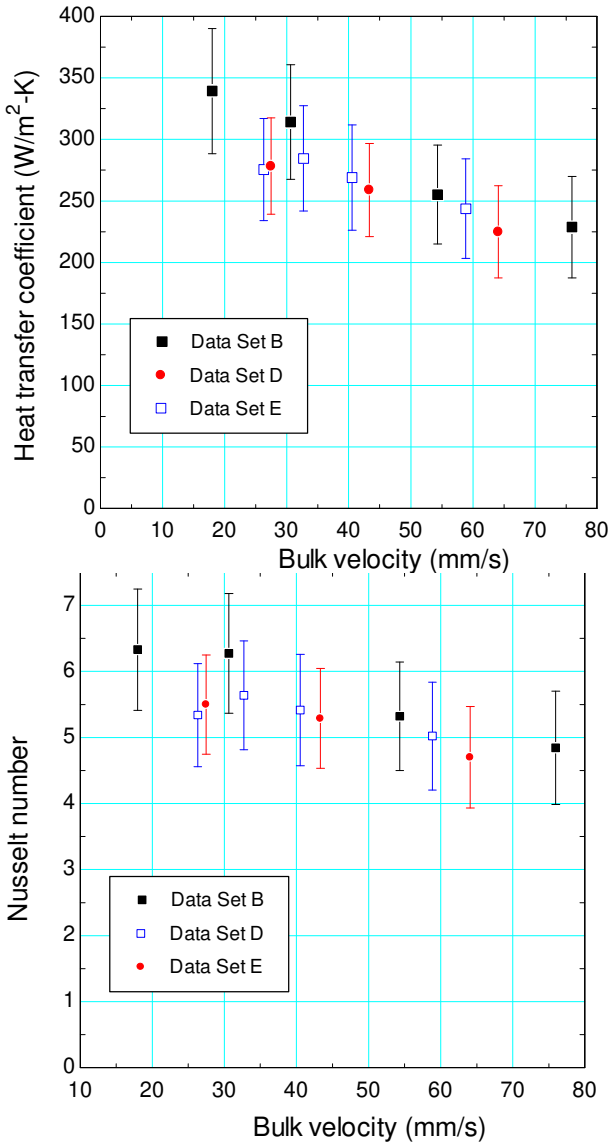

Figure 6: Measured (left) heat transfer coefficient and (right) Nusselt number from data sets B, E, and D (nominal heat flux 8.0 kW/m^2) as a function of bulk velocity.

Data sets A and G both measure the heat transfer coefficient under conditions of varying inlet temperature (obtained through successive preheating cycles). The preheating cycles induce temperature non-uniformities in the inlet hopper that tend to increase the uncertainty in the measurements. Figure 7 shows the measured heat transfer coefficient and Nusselt number as a function of the average temperature in the developing region. Again, the increase in heat transfer coefficient with temperature is mostly explained by the conductivity.

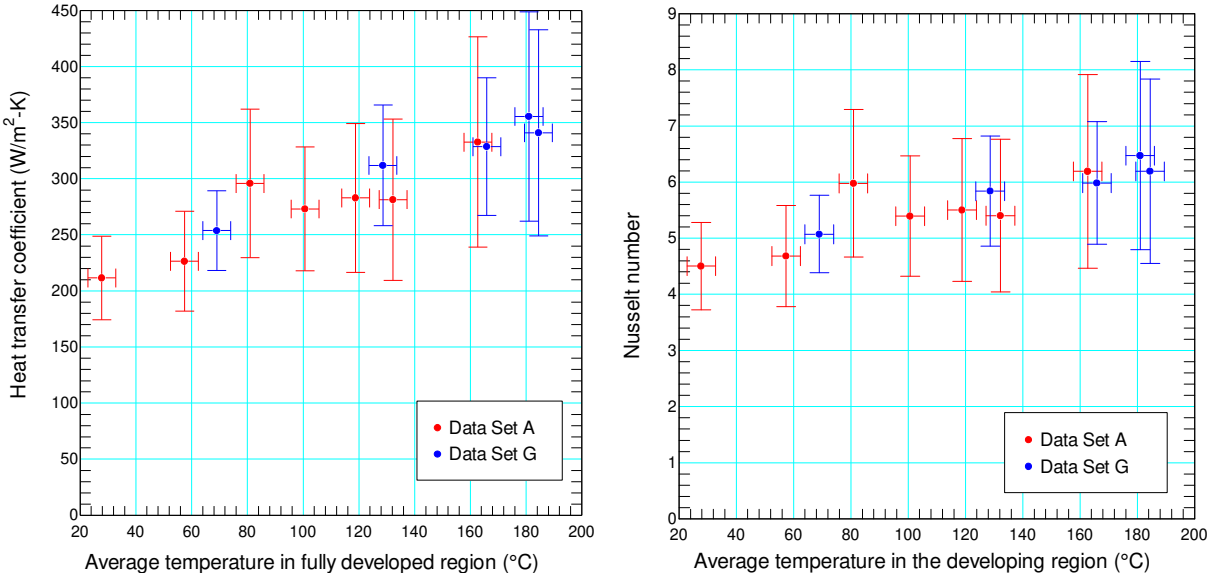

Figure 7: Measured (left) heat transfer coefficient and (right) Nusselt number from data sets A and G (nominal heat flux 7.5 kW/m^2) as a function of average temperature in the developing region.

Finally, data set F measures the heat transfer coefficient as a function of heat flux for nominally constant inlet temperature and flow rate. The results are presented in Figure 8; although the uncertainty for the low heat flux runs is high due to the small temperature differences that are produced there does not seem to be any significant effect of heat flux.

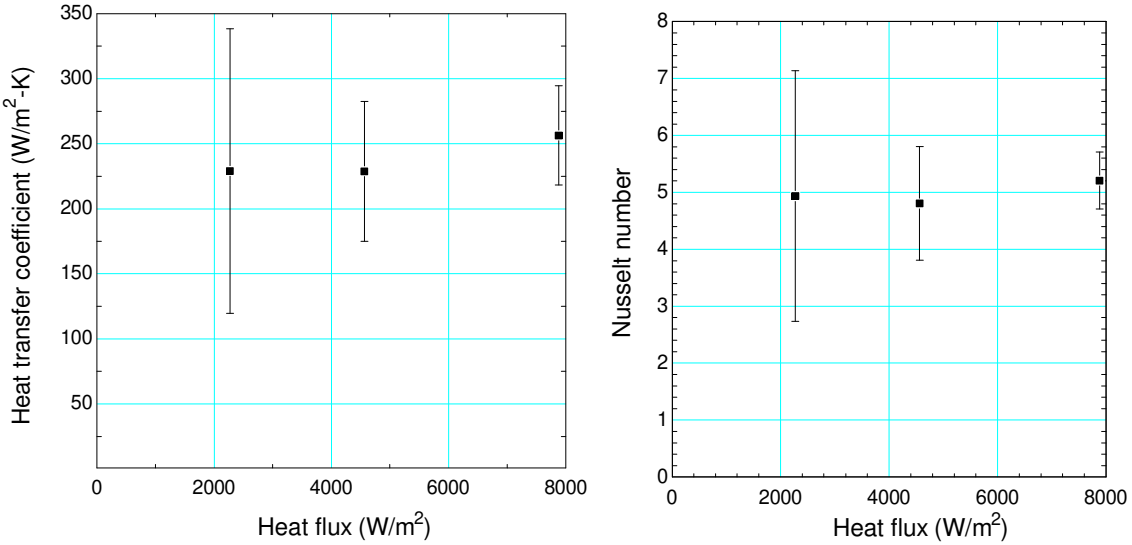

Figure 8: Measured (left) heat transfer coefficient and (right) Nusselt number from data set F (nominal bulk velocity 31 mm/s) as a function of heat flux.

4. Discussion

Several researchers (e.g., Brinn et al., 1948 and Watkins, 2018) have shown that particle flow in an uninterrupted channel behaves like plug flow hydrodynamically, but with an additional

thermal resistance associated with the high porosity region of particles near the wall. The fully developed Nusselt number for laminar fully developed slug flow in the channel formed by parallel plates with a constant heat flux boundary condition is 12 (Muzychka et al., 2010). In this experiment, only one wall is heated and therefore we would expect that the unheated surface behaves like the adiabatic centerline of a channel with both surfaces heated. As a result, the fully developed Nusselt number for this experiment should be Nu_{fd} = 6.0. Examining Figures 6-8 shows that the measured Nusselt number is consistently somewhat less than 6.0; this is likely due to the additional thermal resistance that is associated with the relatively high void fraction in the region near the wall.

Several researchers have suggested that the wall effect can be approximately modeled as a contact resistance that acts in series with the typical fluid-to-surface heat transfer coefficient. The area-specific contact resistance associated with the experiments described here can be estimated as:

$$R_c'' = \frac{1}{h} - \frac{2g}{Nu_{fd}\,k} \tag{11}$$

The most precise measurements of the heat transfer coefficient were those taken with no preheating and at relatively high heat flux and high velocity. These data points were used to compute the experimental area-specific contact resistance at each location and the results are shown in Figure 9 (left) as a histogram. Figure 9 (right) shows the calculated area-specific contact resistance from data sets B, E, and D which provide data over a range of bulk velocity. As previously seen in Figure 6 (right), the data appears to show an increased effect of the wall adjacent layer with velocity; this effect has been suggested by Watkins (2018) due to a reduction in packing fraction and wall contact.

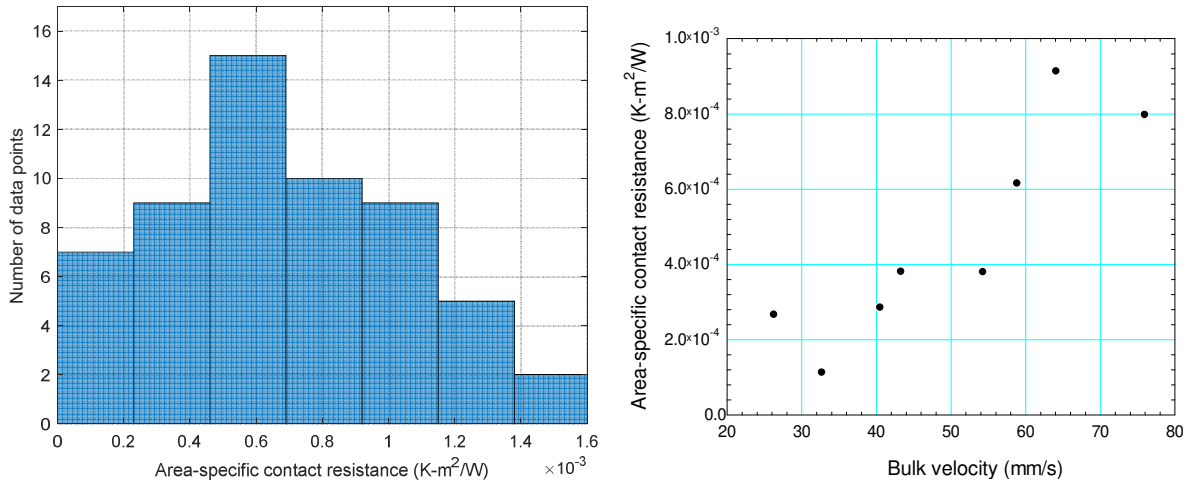

Figure 9: (left) Histogram of area-specific contact resistance calculated from high velocity, high heat flux data with no pre-heating and (right) area-specific contact resistance as a function of bulk velocity from data sets B, E, and D (nominal heat flux 8.0 kW/m^2).

The average area-specific contact resistance from all of the data is R_c'' = 6.8x10^{-4} K-m^2/W. The calculation of area-specific contact resistance using Eq. (11) is the difference between two relatively large numbers and therefore there is substantial scatter in the results. There is a substantial amount of work devoted to empirically and theoretically quantifying the impact of the wall-adjacent layer. The values measured here are approximately consistent with the model presented by Albrecht and Ho, 2017, which is reprinted below for convenience. The contact resistance calculated using the model will be designated as $R_{c,a}''$ to differentiate it from R_c'', the value determined from the data.

$$R_{c,a}'' = \frac{d_p}{2k_{nw}} \tag{12}$$

where d_p is the particle diameter (taken to be the Sauter mean diameter) and k_{nw} is the effective thermal conductivity in the near wall region, calculated according to:

$$k_{nw} = k_g \left[\varepsilon_{nw} + \frac{1-\varepsilon_{nw}}{2\Phi + \frac{2k_g}{3k_s}} \right] \tag{13}$$

The parameter ε_{nw} is the near-wall porosity, which can be computed for a flat plate according to:

$$\varepsilon_{nw} = 1 - 0.7293\left(1-\varepsilon_s\right) \tag{14}$$

where ε_s is the porosity in the bulk (38%). The parameters k_g and k_s are the conductivity of the gas phase and solid phase, and Φ is the ratio of the effective thickness of the fluid film to the particle diameter (Botterill and Denloye, 1978):

$$\Phi = \frac{1}{4}\left[\frac{\left((K-1)/K\right)^2}{\ln\left(K\right) - \left(K-1\right)/K} \right] - \frac{1}{3K} \tag{15}$$

where $K = k_s/k_g$. The result of applying Eqs. (12) through (15) for the conditions that are used in this experiment is $R_{c,a}''$ = 1.2x10^{-3} K-m^2/W; this value is about 75% higher than the average of the experimentally determined values found in Figure 9. Using $R_{c,a}''$ = 1.2x10^{-3} K-m^2/W leads to a Nusselt number of approximately 4.6 under the conditions associated with data sets B, E, and D which slightly under-predicts the experimental results, as shown in Figure 10.

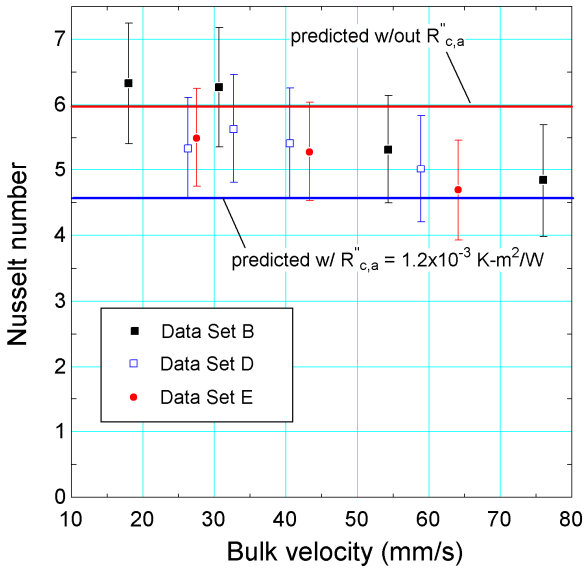

Figure 10: Measured Nusselt number from data sets B, E, and D (nominal heat flux 8.0 kW/m^2) as a function of bulk velocity. Also shown is the fully developed Nusselt number predicted with no wall-adjacent contact resistance and the fully developed Nusselt number calculated using the wall-adjacent contact resistance predicted by Eqs. (12) – (15).

There is a substantial amount of work related to empirically and theoretically quantifying the impact of the wall-adjacent layer; however, the model developed by Albrecht and Ho, 2017, provides a relatively straightforward method for estimating this effect. As a result, it can be integrated into heat exchanger design calculations as shown in Albrecht and Ho, 2019. These data indicate that this model provides a reasonable, if possibly slightly high, estimate of the thermal resistance.

5. Conclusions

This paper describes an experimental test facility capable of measuring the heat transfer coefficient associated with a fully developed moving bed flow through the channel formed by two parallel plates with one heated. The results, when non-dimensionalized and presented as a Nusselt number, are shown to be relatively insensitive to heat flux and temperature over the temperature range used in the experiments (0ºC - 200ºC) and weakly dependent on velocity. The measured results are slightly lower than the theoretically predicted Nusselt number for fully developed laminar slug flow under the same conditions. The difference is likely due to a thermal resistance related to the near wall region which has relatively higher porosity. The area-specific thermal contact resistance which would account for the discrepancy was computed for the highest quality data points and found to be similar, but smaller than the value suggested by one model in the literature. The specific thermal contact resistance was also found to be dependent on the bulk velocity. Future work should be directed toward understanding particle flow behavior through more complex geometries that will be necessary to improve the economics of the particle-to-fluid heat exchangers in thermal energy systems.

6. Acknowledgements

This work was funded by the Department of Energy's Office of Energy Efficiency and Renewable Energy under award DE-EE0008368 through a subcontract from Brayton Energy. This research was partially supported by the University of Wisconsin-Madison College of Engineering Shared Research Facilities and the NSF through the Materials Science Research Center (DMR-1720415) using instrumentation provided at the UW-Madison Materials Science Center.

7. Nomenclature

c	specific heat capacity (J/kg-K)
d_p	particle diameter (m)
k	conductivity (W/m-K)
g	gap height (m)
h	heat transfer coefficient (W/m^2-K)
i	enthalpy (J/kg)
K	ratio of solid to gas conductivities (-)
L	channel length (m)
$\dot{m}$	mass flow rate (kg/s)
Nu	Nusselt number (-)
$\dot{q}$	rate of heat transfer (W)
$\dot{q}''$	rate of heat transfer per unit area (W/m^2)
R_c''	area-specific contact resistance (K-m^2/W)
T	temperature (ºC)
u	bulk velocity (m/s)
W	gap width (m)
x	axial location (m)

Roman symbols

ε	porosity (-)
Φ	parameter in equation for near wall conductivity (-)
ρ	density (kg/m^3)

Subscripts

a	analytical
C	unheated surface
e	electrical
fd	fully developed
g	gas-phase
H	heated surface
in	inlet
nw	near-wall
out	outlet
s	surface or solid-phase

t thermal

8. References

Alaqel, S., A. El-Leathy, H. Al-Ansary, E. Djajadiwinata, N. Saleh, S. Danish, R. Saeed, A. Alswaiyd, Z. Al-Suhaibani, S. Jeter, A. Al-Balawi, and F. Al-Harthi, 2020, Experimental investigation of a shell-and-tube particle-to-air heat exchanger, Solar Energy, 204, 561-568.

Albrecht, K.J. and C.K. Ho, 2017, Heat Transfer Models of Moving Packed-Bed Particle-to-SCO_2 Heat Exchangers, Proc. of the 2017 Power and Energy Conference, June 25-30.

Albrecht, K.J., Ho, C.K., 2018, High-Temperature Flow Testing and Heat Transfer for a Moving Packed-Bed Particle/sCO_2 Heat Exchanger, AIP Conference Proceedings 2033, 040003.

Albrecht, K.J., Ho, C.K., 2019, Design and operating considerations for a shell-and-plate, moving packed-bed, particle-to-sCO_2 heat exchanger, Solar Energy, 178, 331-340.

Baskakov, A.P., 1964, The mechanism of heat transfer between a fluidized bed and a surface, *Int. Chem. Eng.,* 4, 320-324.

Baumann, T., and S. Zunft, 2015, Development and performance assessment of a moving bed heat exchanger for solar central receiver plants, Energy Procedia, 69, 748-757.

Botterill, J.S.M. and A.O.O. Denloye, 1978, A Theoretical Model of Heat Transfer to a Packed or Quiescent Fluidized Bed, Chemical Engineering Science, 33, 509-515.

Brinn, M.S., S.J. Friedman, F.A. Gluckert, and R.L. Pigford, "Heat Transfer to Granular Materials," *Ind. Eng. Chem.*, Vol 40 (6), pp. 1050-1061, (1948).

Byman, A.D., Charles, T.L., Huang, X., 2014, U.S. Patent No. US20140246184.

Cundal, P.A. and O.D.L. Strack, 1979, A discrete numerical model for granular assemblies, Géotechnique, 29, 47-65.

Fairmount Mineral's Wedron Silica Sand data sheet, https://jandsnewsite.files.wordpress.com/2019/03/silica-sand-tech.pdf , accessed on 1/13/22.

Gomez-Garcia, F., Gauthier, D., Flamant, G., 2017, Design and performance of a multi-stage fluidized bed heat exchanger for particle-receiver solar power plants with storage, Applied Energy, 190, 510-523.

Ho, C.K., Carlson, M., Albrecht, K.J., Ma, Z., Jeter, S., Nguyen, C.M., 2018, "Evaluation of Alternative Designs for a High Temperature Particle-to-SCO2 Heat Exchanger," Proc. 2018 Power & Energy Conf, June 24-28.

Kirschmeier, M.F., Boxleitner, J., Corbeil, A, Sullivan, S, 2020, Design of a Novel Counterflow Particle-to-sCO_2 Heat Exchanger, Proc. of the 2020 SolarPACES Conference.

Maskalunas, J., 2020, High-Temperature Thermal Properties of Particles for Concentrated Solar Power and Thermal Energy Systems, M.S. Thesis, Mechanical Engineering Department, University of Wisconsin, Madison.

Maskalunas, J., G. Nellis, and M. Anderson, 2020, High-Temperature Thermal Properties of Particles in Consideration for Thermal Storage in Concentrated Solar Power Systems, Proceedings of the 26th SolarPACES Conference.

Morris, A.B., S. Pannala, Z. Ma, and C.M. Hrenya, 2015, A conductive heat transfer model for particle flows over immersed surfaces, Int. J. Heat Mass Transfer, 89, 1277-1289.

Morris, A.B., Z. Ma, S. Pannala, and C.M. Hrenya, 2016, Simulations of heat transfer to solid particles flowing through an array of heated tubes, Solar Energy, 130, 101-115.

Muzychka, Y.S., E. Walsh, and P. Walsch, 2010, Simple Models for Laminar Thermally Developing Slug Flow in Noncircular Ducts and Channels, Journal of Heat Transfer, 21.

NIST-JANAF Thermochemical Tables,, National Institute of Standards and Technology, (1998), at: https://janaf.nist.gov/ (accessed on 12/2020).

Schlünder, E.U, 1982, Particle Heat Transfer, Proc. of the 7th Int. Heat Transfer Conference, 195-211.

Tsotsas, E., 2010, Heat transfer from a wall to stagnant and mechanically agitated beds, in Heat Atlas, 2nd Edition, V.D.I. Gesellschaft, ed. Springer, Dusseldorf, 1311-1326.

van Antwerpen, W, C.D. Toit, and P. Rousseau, 2010, A review of correlations to model the packing structure and effective thermal conductivity in packed beds of mono-sized spherical particles, Nuclear Engineering and Design, 240, 1803-1818.

Watkins, M.F., 2018, A Heat Transfer Analysis of Vertical Dense Granular Flows, Ph.D. Thesis, Mechanical Engineering Department, North Carolina State University.